Structure–property relationships in (1 − x)BaTiO3–xBiGdO3 ceramics

SCHILEO, Giorgio, FETEIRA, Antonio <http://orcid.org/0000-0001-8151-7009>, REICHMANN, Klaus, LI, Ming and SINCLAIR, Derek

Structure-property relationships in (1-x)BaTiO$_3$-xBiGdO$_3$ ceramics

Giorgio Schileo[1], Antonio Feteira[1], Klaus Reichmann[2], Ming Li[3] and Derek C. Sinclair[3]

[1]Christian Doppler Laboratory for Advanced Ferroic Oxides, Sheffield Hallam University, Howard Street, S11WB, Sheffield, U.K.

[2]Christian Doppler Laboratory for Advanced Ferroic Oxides, Institute for Chemistry and Technology of Materials, Graz University of Technology, Stremayrgasse 9, Graz, A-8010, Austria

[3]Department of Materials Science and Engineering, The University of Sheffield, Mappin Street, S1 3JD, Sheffield, U.K.

Abstract

(1-x)BaTiO$_3$-xBiGdO$_3$ ceramics were prepared by the solid state reaction method. X-ray diffraction and Raman spectroscopy indicate a maximum co-solubility of Bi/Gd in BaTiO$_3$ at x = 0.10 with a change of symmetry from tetragonal to pseudo-cubic at x = 0.08. Backscattered electron images, however, reveal the presence of a secondary phase in x ≥ 0.06. The dielectric behaviour evolves continuously with x from a classical ferroelectric to a typical relaxor and this transition is accompanied by a shift in the permittivity maxima towards lower temperatures. The presence of two dielectric anomalies for x ≥ 0.06 is associated with residual core–shell structures, as revealed by transmission electron microscopy. The dielectric anomaly associated with the core regions remains at ∼120 °C, whereas the other anomaly decreases continuously towards lower temperature with x. This study shows that chemical equilibrium is much more difficult to achieve than in other (1-x)BaTiO$_3$-xBi[Me]O$_3$ systems, where Me is Yb or Sc.

I-Introduction

BaTiO$_3$ (BT) is a well-known ferroelectric perovskite [1] that is widely used in the manufacture of multilayer ceramic capacitors mainly due to its inherent large relative permittivity at room temperature (ε_r ~1600) [2]. Above its Curie temperature, T$_C$ (~ 130 °C) the crystal structure symmetry is pseudo-cubic (space group $Pm\bar{3}m$). On cooling, it undergoes three consecutive structural phase transitions, at 130 °C from pseudo-cubic to tetragonal ($P4mm$), at 0 °C from tetragonal to orthorhombic ($Amm2$) and at -90 °C from orthorhombic to rhombohedral ($R3c$).All transitions encompass a second-order Jahn-Teller distortion involving hybridisation between the Ti 3d and O 2p orbitals, causing a displacement of Ti^{4+} with respect to the anions, thereby leading to the appearance of spontaneous polarisation along different crystallographic directions [3,4]. These transitions manifest themselves as dielectric anomalies (maxima) on the temperature dependence of the relative permittivity, ε_r. The ferroelectric-to-paraelectric transition at 130 °C is accompanied by a sharp peak in ε_r, which reach values as high as ~10, 000-12, 000, depending on microstructure [5,6]. This large temperature dependence of ε_r is undesirable for most of its technological applications. Chemical doping can be used to shift T$_C$ and to broaden the temperature dependence of ε_r. Indeed, the vast majority of dopants lower and broaden the T$_C$ maximum (with a few exceptions like Pb^{2+} and Ca^{2+}) because they interfere with the long-range ordering of dipoles [7].

Simultaneous replacement of Ba^{2+} by Bi^{3+} and Ti^{4+} by a trivalent metal for charge compensation has been studied in recent years. Bi^{3+}, like Pb^{2+}, possesses a $6s^2$ lone pair of electrons which is not involved in any chemical bonds. This lone pair is highly polarizable and it has been demonstrated, *e.g.* in compounds such as BiFeO$_3$ and BiMnO$_3$, a long-range ordering of lone pairs can provide an alternative source for the occurrence of ferroelectricity [4]. Another reason why Bi doping of BT is currently under investigation concerns the search for lead-free ceramics to comply with new European regulations aiming at the gradual replacement of lead in electronics, due to its toxicity. Bi has been used as dopant in BT in combination with Al, Sc, In and Yb [8-11].

BiAlO$_3$ is thermally unstable and decomposes at 550 °C, just 30 °C above its T$_C$ of 520 °C. BiAlO$_3$ solid solution limit with BaTiO$_3$ (r$_{Al}$ = 0.535 Å, 11% *smaller* than Ti [12]) was reported to be x ~0.12, with a phase transition from tetragonal to rhombohedral at x ~0.10. Nevertheless, the composition x = 0.15 was also investigated and described as a typical relaxor, even if a more diffuse character of the dielectric peak starts to appear at x = 0.10, together with the so-called "pinching" of phase transitions (the gradual merging of all three phase transitions in pure BT in one single

broad peak in doped BT). $(1-x)BaTiO_3-xBiScO_3$ solid solution (r_{Sc} = 0.745 Å [12]) presents a phase transition from tetragonal to pseudocubic at $x \sim 0.05-0.075$. The lattice parameters follow the empirical Vegard's law and no signs of secondary phases up to $x = 0.40$; T_C decreases slowly with composition until $x = 0.06$, then more steeply where clear relaxor behaviour is established. With increasing x, the permittivity maximum moves towards higher temperatures.

$BiInO_3$ cannot be prepared at ambient pressure, however Bi (r_{Bi} = 1.45 Å, extrapolated [12]), and In (r_{In} = 0.80 Å [12]) can substitute for Ba and Ti in $BaTiO_3$, respectively, up to $x = 0.25$. In this case, the tetragonal to pseudocubic transition lies between $x = 0.10$ and $x = 0.12$, with the two phases clearly coexisting at $x = 0.10$.

Finally, the $(1-x)BaTiO_3-xBiYbO_3$ system adopts a tetragonal structure which continuously decreases in tetragonality until $x = 0.06$, above which it can be fully indexed as pseudocubic. T_C and the degree of tetragonality decrease accordingly, but above $x = 0.06$ the permittivity maximum shifts again towards higher temperatures.

To the best of our knowledge, the impact of Bi and Gd co-doping on the structure and properties of $BaTiO_3$ has not been reported. Here we use a combination of X-ray diffraction (XRD), Raman spectroscopy, Scanning and Transmission Electron Microscopy, and dielectric measurements to establish the structure-property relationships in ceramics prepared according to the formula $Ba_{1-x}Bi_xTi_{1-x}Gd_xO_3$. $BiGdO_3$ is a putative end-member, as it has never been synthesised under normal ambient pressure. It has been proposed that a hypothetical compound may be stable with the perovskite structure for a tolerance factor, t with $0.88 < t < 1.09$ [13]. The value of t for the end-member $BiGdO_3$ is below the lower limit (0.862). In fact, it is much smaller than the t factor of prototypical perovskites such as $BaTiO_3$ and $SrTiO_3$ (1.062 and 1.002, respectively).

II-Experimental

$BaCO_3$ (Sigma-Aldrich, UK ACS reagent, >99%), TiO_2 (Sigma-Aldrich, UK, ACS reagent, >99%), Gd_2O_3 (Sigma-Aldrich, UK, ACS reagent, 99.9%), Bi_2O_3 (Sigma-Aldrich, UK, ACS reagent, 99.9%) were weighed according to the $(1-x)BaTiO_3-xBiGdO_3$ stoichiometry to obtain solid solutions with $0.00 \leq x \leq 0.15$, and ball milled overnight with propan-2-ol using yttria-stabilised zirconia milling media. The obtained slurries were dried at 80 °C and fired consecutively at 800, 900 and 1000 °C for 8 hours, with intermediate milling cycles between each calcination. Calcination at 1000 °C was repeated until no changes were observed in x-ray diffraction (XRD) data. The calcined powders were mixed with 5%w polyethylene glycol to improve the mechanical strength of the green bodies. Pellets

3

of 13 mm in diameter were uniaxially pressed in a stainless steel die (Specac, Kent, UK) under an applied pressure of 50-100 MPa. The final sintering was carried out between 1350 °C (for $0.00 \leq x \leq 0.06$) and 1400 °C (for $0.08 \leq x \leq 0.15$) for 2 h, in a closed crucible and covering the pellets with source powder of the same composition. The firing profile included a de-binding step using a heating rate of 1 °C/min up to 350 °C followed by heating at 5 °C/min to the sintering temperature.

Room-temperature XRD patterns were recorded with an X-ray diffractometer in transmission geometry (model: AXS D8 Advance, Bruker™, Coventry, UK) using Kα-Cu line at λ = 1.54059 Å and a step size of 0.02°. Rietveld refinements were performed with the General Structure Analysis System (GSAS) suite of programs [14]; a polynomial function of up to 7 terms was used to fit the background, whereas a pseudo-Voigt function was chosen to fit the peaks. Thermal displacement parameters were set to isotropic. Silicon powder (99.999%, Alpha Aesar, 325 mesh, lot no. 5001L26T) was mixed together with the samples and used as reference material. The Si cell parameters were fixed while the zero correction in GSAS was varied to best fit them [15]. Raman spectra were obtained with a Raman Microscope (model: inVia, Renishaw™, New Mills, UK) in backscattering geometry and a 532 nm non-polarized Argon laser light using an objective lens of 20× and 50× magnification.

Relative permittivity measurements above room temperature were carried out with an Impedance/Gain Phase Analyser (model: 1260, Solartron Instruments, Farnborough, UK) coupled to a tube furnace (model: MTF, Carbolite, Hope Valley, UK). Sub-ambient measurements were performed using an LCR meter (Agilent E4980A, Agilent, USA) in a closed-cycle He refrigerator (Oxford Instruments Ltd., Oxfordshire, UK). The sintered pellets were coated with Pt or Ag paste. Capacitance was measured versus temperature (from 300 to 520 K and from 10 to 300 K at 2 K intervals) at four different frequencies (1, 10, 100 and 1000 kHz). Sintered pellets were polished using SiC sandpaper and 6 and 1 µm diamond paste polishing pads, and subsequently thermally etched at 1200 ºC for 30 minutes.

Ceramic microstructures were investigated using Scanning Electron Microscopes (SEM) (Model: XL30 with LaB₆ crystal, Philips, The Netherlands and model: Nova Nano 200 with a Field Emission Gun, FEI, Czech Republic) operated at 20 kV and using a 5 to 10 mm working distance. SEM micrographs were taken from both polished and fractured surfaces. Samples were examined in both Secondary Electron (SE) and BackScattered Electron (BSE) imaging modes. Chemical microanalysis were carried out by Energy Dispersive X-ray spectroscopy (EDS). EDS signals were optimised for the best signal-to-noise ratio and collected for 60 s (at each point). For TEM analysis, the

4

ceramics were ground manually with SiC sandpaper until about 80 μm, mounted on copper rings, fixed with epoxy resin and bombarded with Ar ions for 3 hours using a Precision Ion Polishing System (PIPS^{TM}) (model 691, Gatan, Abingdon, UK) operating at a milling angle of ± 8° and beam energy of 4 keV. A TEM (model CM20, Philips, The Netherlands) equipped with a tungsten filament and operated at an accelerating voltage of 200 kV was used for examining the grain substructure.

III-Results

Structure and Purity

Room-temperature XRD patterns for $(1-x)$BaTiO$_3$-xBiGdO$_3$ ($0 \leq x \leq 0.15$) powders are shown in Fig. 1a. For $x \leq 0.10$, all reflections shift towards lower 2θ with increasing x, indicating an increase in unit cell volume. In addition, splitting of doublet reflections such as (200)/(002) gradually decreases with increasing x, indicating a reduction in the degree of the tetragonal distortion, Fig. 1b. For $x \leq 0.06$, diffraction data can be indexed on a tetragonal structure (space group $P4mm$), whereas for $x \geq 0.10$ the average crystal symmetry appears to be consistent with a cubic perovskite (space group $Pm\bar{3}m$). Tetragonal and cubic symmetries coexist for $x = 0.08$. No super-lattice reflections that may indicate the presence of octahedral tilting or cation ordering were detected, but a minor secondary phase was detected, as indicated by the asterisk in Fig. 1. The extra peaks match well the XRD pattern of Bi$_{1.55}$Gd$_{0.45}$O$_3$ (PDF no. 00-048-0351).

Lattice parameters calculated from the Rietveld refinements are listed in Table 1. The unit cell volume increases almost linearly up to $x = 0.10$ and then reaches a plateau, suggesting the solid solution limit has been achieved, Fig. 2. The compositional variation of the unit cell volume is compared with results for $(1-x)$BaTiO$_3$-xBiYbO$_3$ [11] in Fig. 3. The volumes start to diverge at $x \geq 0.02$. Moreover and rather surprising, the unit cell volume for the Gd-series appears smaller than that for the Yb-series counterparts. This result is contrary to expectation because Gd has a larger ionic radius than Yb, and its incorporation on the B-site should produce a larger unit cell. Nevertheless, Rietveld refinement shows evidence for Bi (A-site) vacancies, especially for higher dopants concentrations. χ^2 (goodness of fit) slightly improves if the occupancy of A-sites is lower than its theoretical value. However, χ^2 for some compositions could not be reduced below 3, therefore any conclusion from the fitting of the data must be drawn with caution.

Raman Spectroscopy

Raman spectroscopy has a shorter length of scale than XRD, therefore it allows the identification of local deformations arising from the difference between the ionic radii of the dopants and of the ions that they replace [16]. In pure, polycrystalline $BaTiO_3$ there are three broad modes at about 260 cm^{-1} [A_1(TO)], 520 cm^{-1} [A_1(TO)] and 720 cm^{-1} [A_1(LO)], a dip at 180 cm^{-1}[A1+E] and a sharp peak at 307 cm^{-1}[E(TO)] [11]. The sharp peak at 307 cm^{-1} is commonly regarded as a "signature" of ferroelectric behaviour (long-range ordering of dipoles) in $BaTiO_3$[17]. The room temperature Raman spectra for $Ba_{1-x}Bi_xTi_{1-x}Gd_xO_3$, Fig. 4, show that small concentrations of Bi and Gd have a dramatic impact on the observable modes. In particular, the sharp peak at ~307 cm^{-1} starts to broaden for $x = 0.02$ and eventually disappears at $x = 0.08$. The dip around 182 cm^{-1} in pure $BaTiO_3$ is also affected by small amounts of Bi/Gd and disappears at $x = 0.04$. Probably the most important feature is the extra band at about 830 cm^{-1}, whose intensity is proportional to the dopant concentration, and a new mode above 180 cm^{-1}; the latter was previously observed in the $BaTiO_3$-$BiYbO_3$ when the average crystal symmetry changed from tetragonal to pseudocubic [11]. The compositional dependence of the phonon modes is illustrated in Fig. 5. The A_1(TO) mode at 260 cm^{-1} continuously hardens up to $x = 0.08$, whereas the A_1(LO) mode at 720 cm^{-1} shows a frequency inflection at this concentration. This variation reflects the change of the average crystal symmetry observed from the XRD data. The new modes, 1 and 2, soften continuously with increasing x, which may be associated with the increase in unit cell volume.

Ceramic Microstructure and Phase Assemblage

Microstructure and phase assemblage were investigated by SEM with BSE images used to identify any compositional inhomogeneity and EDS employed to estimate chemical composition(s), as appropriate. In undoped $BaTiO_3$ the grain size reaches 10-20 µm [18], Fig. 6.a; grain growth is inhibited upon incorporation of small amount of dopants: for $0.02 \leq x \leq 0.06$, the grain size distribution appears quite narrow with most grains ranging from 1 µm (or even less) to about 3 µm, Fig. 6b-d. Although $x = 0.02$ appears dense, the number and the size of pores in $x \geq 0.04$ ceramics appears to increase. BSE images revealed a very small amount of parasitic phase in $x = 0.04$ (Fig. 6c) that could not

be detected by XRD. EDS analysis performed on 10 points starting from the central plane of the cross-section towards the surface for $x = 0.02$ and 0.08 did not show any evidence of compositional gradients. In both samples, the composition in the centre matched the composition near the surface, especially for the value of Bi. Pores > 5 µm were observed on the polished cross-section of $x = 0.08$ ceramics, whereas the grain size distribution remained between 1 and 5 µm. For $0.10 \leq x \leq 0.15$, large pores (5-10 µm) were visible across the surface of as-fired ceramics; after grinding those surfaces samples were re-examined and the high degree of porosity remained, indicating that bulk porosity is an inherent feature in those ceramics. This observation corroborates the low values of relative density measured for these ceramics (~90%). Also, the presence of the parasitic phase (bright areas between grains) was more evident in $0.08 \leq x \leq 0.15$, as shown by the BSE images. For $0.10 \leq x \leq 0.15$, the grain size distribution narrowed slightly, as smaller grains coalesced into ~5 µm grains, and the intergranular space between the grains became almost completely filled by the Bi and Gd enriched secondary phase, Fig. 6, e-g. EDS analysis on the secondary phase is listed in Table 2.

Bright-field TEM of $x = 0.10$ revealed the presence of a core/shell structure, as illustrated in Fig. 7. The outer region of the grains showed the typical mottled contrast commonly exhibited by relaxors. A similar observation was reported by Ogihara *et al.*[9] for $(1-x)$BaTiO$_3$-xBiScO$_3$ ceramics.

Dielectric properties

The temperature dependence of ε_r for $(1-x)$BaTiO$_3$-xBiGdO$_3$ ceramics is shown in Fig. 8. The permittivity maximum, ε_{max}, broadens and shifts towards lower temperature with increasing x; up to $x = 0.06$ (Fig. 8.d) typical ferroelectric behaviour is observed, whereas the system evolves into a relaxor for $x \geq 0.10$; for $x = 0.08$ there are two dielectric anomalies, ascribable to the ferroelectric and the relaxor phase (see Fig. 8.e). This is consistent with the XRD patterns, where the system transforms from tetragonal to pseudocubic with the coexistence of the two phases, Fig.1.b. The value of the dielectric permittivity maximum, ε_{max}, decreases from ~4000 for $0.02 \leq x \leq 0.06$ to ~2000 for $x \geq 0.10$, whereas the dielectric loss is 10% or lower for most frequencies and compositions. Thus, according to the overall dielectric behaviour, $(1-x)$BaTiO$_3$-xBiGdO$_3$ceramics can be divided into two groups: for $0.02 \leq x \leq 0.06$ only one dielectric anomaly is detectable, whereas for $x \geq 0.08$ a second maximum is visible. The first anomaly is

composition-dependent and therefore shifts to lower temperature with increasing x at ~ 10 °C/mol, the other anomaly remains constant at T ~130 °C. The latter is smaller in magnitude due to the small amount of ferroelectric phase still present in $x = 0.10$ and $x = 0.15$, Fig. 8.g.

IV-Discussion

<u>**Structure and Purity**</u>

XRD data indicate $x = 0.10$ as the solid solution limit for this system. Based on reported data for $Ba_{1-x}Bi_xTi_{1-x}[\textbf{Me}^{\textbf{III}}]_xO_3$ solid solutions (where $\textbf{Me}^{\textbf{III}}$ is a trivalent metal) the solid solution limit may depend (among other factors) on the ionic radius of the B site dopant: for Al, due to its small size, it is only 12%, it then reaches a maximum at 40% for Sc before decreasing again for the larger Yb (30%), Table 3.

From additional XRD patterns taken at intermediate stages during the fabrication process it was possible to follow the evolution of parasitic phases with processing temperature, Fig. 9. At 800 °C unreacted Bi_2O_3 (PDF no. 01-076-2478) was still present, alongside with Gd_2TiO_5 (PDF no. 00-034-1307). After milling and re-firing up to 1000 °C, a stable phase forms: $Bi_{1.208}Gd_{0.792}O_3$ (PDF no. 00-040-0318). To promote complete reaction into a single phase, the sintering temperature was increased to 1400 °C. At this stage however, a small amount of parasitic phase remained observable on a logarithmic scale (Figs. 1 and 9). This phase was identified as $Bi_{1.55}Gd_{0.45}O_3$ (PDF no. 00-048-0351), which - compared to $Bi_{1.208}Gd_{0.792}O_3$- presents a higher Bi-to-Gd ratio; the peak positions of the $BaTiO_3$ doped lattice shift towards lower angles after sintering at 1400 °C: the (001)/(100) reflection shifts from 22.101 ° to 21.980 °, (110) from 31.349 ° to 31.295 °, and (111) from 38.712 ° to 38.586 °. This indicates that at least some Gd from the parasitic phase has become incorporated into the $BaTiO_3$ lattice.

Although the unit cell volume increases with x, as illustrated in Fig. 2, based on ion size arguments this is not as high as expected when compared to the compositional dependence of Bi/Yb-doped $BaTiO_3$, given that Gd^{3+} in 6-fold coordination is ~8% larger than Yb^{3+}[12], Fig. 3. This can be interpreted by incomplete incorporation of Bi and/or Gd. Alternatively, Gd may occupy simultaneously both the A and B sites of the $BaTiO_3$ lattice. In fact, *ab initio* calculations indicate that Gd^{3+} can occupy both A and B sites, leading to a self-compensation mechanism. In the present case, Gd^{3+} may enter the A site, due to a relatively slow incorporation of Bi and/or its volatilisation at high

8

temperatures, however Rietveld refinement also shows evidence for Bi (A site) vacancies, especially for higher dopants concentrations. χ^2 (goodness of fit) for some compositions could not be reduced below 3, maybe due to unaccounted residual lattice stress, the small size of the nanodomains in the relaxor compositions or the presence of the secondary parasitic phase. All these factors can affect peak shape and therefore the quality of the fit.

Dielectric properties

The ferroelectric-to-relaxor crossover due to the increasing amount of dopants in the $BaTiO_3$ matrix can be followed by the evolution in the dielectric behaviour, Raman spectra and XRD patterns. All these techniques allowed two regimes to be identified: in the first one, up to $x = 0.06$, the global crystal structure remains tetragonal at room temperature, as confirmed by the presence of a sharp peak at 307 cm^{-1} in the Raman spectra, the splitting of the (200)/(002) doublet in XRD data and from the temperature dependence of the permittivity. Higher levels of dopants however cause a series of effects on both the overall and local crystal structure: typical relaxor dielectric behaviour is observed, and both Raman spectra and XRD data indicate a change from tetragonal to cubic symmetry starting at $x = 0.08$, where these two phases coexist (see Fig. 1.b); the structure is referred to as *pseudo*-cubic, since it has been demonstrated that (even if on a time-averaged scale) the position of the Ti^{4+} cation within the oxygen octahedra is in the centre, this situation is better described as a double-well potential, i.e., at $T > T_C$ the thermal energy is sufficient to allow the Ti atom to switch between eight degenerate positions, off-centre with respect to the oxygen framework [18]. This is the reason why the two A_1 bands at 260 and 520 cm^{-1} are still present above T_C even though they should be prohibited in a true cubic phase by Raman selection rules based only on symmetry. It is worth noticing that the A_1(TO) mode at 250-270 cm^{-1}, like - to a less extent - the A_1, E(TO) mode at 510-520 cm^{-1} in undoped $BaTiO_3$ shifts towards higher wavenumbers with Bi^{3+} addition, as reported by Strathdee *et al.*[11], whereas it shifts towards lower wavenumbers upon the addition of La^{3+} as pointed out by Feteira and Sinclair [5]. This effect may be due to the lone pair of electrons on the Bi^{3+} ions. The two modes at 513 and 718 cm^{-1} shift towards higher wavenumbers as already reported for similar perovskite solid solutions [5,11], and therefore may be dependent on the simple dimensions of the unit cell, regardless of the nature of the dopants. The appearance of the new mode (no. 3, see Fig. 4) at about 830 cm^{-1} is clearly related to doping on the B site, as previously reported for Zr-doped BT (BaZr$_x$Ti$_{1-x}$O$_3$) [19]and (*1-x*)BaTiO$_3$-*x*LaYbO$_3$ solid solutions [5], since its intensity increases with the dopant level.

Phase assemblage

EDS results are presented in Table 2. The values of Bi concentration in the matrix are systematically below the theoretical value; a second phase appears between the grains with a high concentration of Bi and Gd; the results of EDS analysis on these areas in different samples (Table 2.b) do not match with each other, possibly because of the small size of the impurity phase grains and/or local inhomogeneity within the impurity itself, nonetheless they indicate that Bi is far more abundant than Gd, which supports the identification of this phase as $Bi_{1.55}Gd_{0.45}O_3$ by XRD. It can be concluded that a certain amount of Bi and Gd, rather than diffusing in the $BaTiO_3$ matrix, remains in intergranular spaces, even with multiple calcination and intermediate milling steps; the incorporation of Bi is slowed by the presence of a rather stable secondary phase, a fact which is corroborated by the EDS results on a $x = 0.10$ sample sintered at 1200 °C for 2 and 10 hours (Table 2.a). Rietveld refinements indicate only a loss of Bi, since the x-ray diffraction intensity from these impurities is too weak to be detected. The presence of impurity peaks for $0.04 \leq x \leq 0.06$ is only possible to be observed in logarithmic scale. The presence of this secondary phase is therefore undetected, or underestimated, by XRD. Increasing the time of sintering at 1200 °C from 2 to 10 hours increased the density by reducing the porosity and by increasing the grain size but nonetheless a complete homogenisation of Bi and Gd into the BT lattice was not possible. This might be explained with the fact that, unlike other perovskite systems used in solid solutions with $BaTiO_3$, $BiGdO_3$ does not exist as a pure end member with a perovskite structure. However, Su and Virkar [20] in their study of the Bi_2O_3-Gd_2O_3 phase diagram reported the existence of a rhombohedral single phase of Bi_2O_3-Gd_2O_3 when the Gd_2O_3 concentration in Bi_2O_3 is between 18 and 30% at room temperature. The XRD pattern reported for 15%-Gd_2O_3-75% Bi_2O_3 present a strong peak at about 28° (2θ), and the EDS results indicate a relative amount of $23.9 \pm 0.1\%$ of Gd and $70.5 \pm 0.1\%$ of Bi, which supports the identification of the parasitic phase as $Bi_{1.55}Gd_{0.45}O_3$ (Fig. 1). Observing EDS results (Table 2a) a clear trend can be observed, which is consistent with the lattice parameters trend: for all compositions up to $x = 0.10$, the measured content of Gd always matches the theoretical value within experimental error (standard deviation), even if it is not possible to state from EDS if Gd occupy B sites only or also the A site. The amount of Bi is increasing up to x = 0.06, to remain stable even for higher concentrations, and it is below the expected values, which corroborates the hypothesis that part of it remains outside the grains in the secondary phase. At $x = 0.15$, the unit cell volume is not increasing and the values of Gd and Bi in the matrix are the same as those for $x = 0.10$, whereas the secondary phase in the $x = 0.15$ sample is enriched in Bi. This explains why the increase in unit cell volume is smaller than the increase in volume for the Bi-

Yb solid solutions with $BaTiO_3$ (Fig. 3) starting exactly from $x = 0.04$ when the first evidence of the secondary phase appears, even though Yb is ~8% smaller than Gd.

The gradual transformation from prototype ferroelectric to relaxor upon doping is also evident from the temperature dependence of the relative permittivity, Fig. 8: consistent with XRD and Raman data, two regimes are identified: the former up to $x = 0.06$ where there is no frequency dispersion and T_C decreases at approximately 10 °C/mol, the latter starting with $x = 0.10$ showing clear relaxor behaviour. The $x = 0.08$ composition presents an intermediate dielectric response, which reflects the coexistence of tetragonal and pseudocubic phases as previously indicated by XRD analysis. The onset of relaxor behaviour is generally ascribed to the disruption of the long range ordering of TiO_6 octahedra and the formation of polar nanoclusters embedded in a paraelectric matrix. In a few cases this is accompanied by the appearance of core/shell structures, where an almost undoped $BaTiO_3$ core is surrounded by a dopant-enriched shell. This inhomogeneity manifests itself in the temperature dependence of permittivity as also claimed by Ogihara and Randall for xBiScO$_3$-(1-x)BaTiO$_3$ solid solutions [9]. For $0.08 \leq x \leq 0.15$, the dielectric response shows two maxima, one staying at an approximately constant T of 120-130 °C and ascribed to the $BaTiO_3$ core, the other shifting towards lower T with increasing x, as expected for T_C upon the addition of dopants. The size and relative amounts of these polar clusters compared to the matrix may explain why they are not observed by x-ray diffraction. TEM micrographs confirmed the presence of ferroelectric domains in the inner region of grains (Fig. 7), whereas no domains are observed towards the grain boundaries, which might be explained by the fact that dopants diffuse into the outer regions only, forming a shell and leaving a ferroelectric core, which is responsible for the dielectric anomaly at ~130 °C. Raman spectroscopy also corroborates these findings: a marked difference between the two groups is shown in Fig. 4. The gradual disappearance of the mode at 307 cm^{-1} (which is commonly regarded as indicator of long-range ferroelectric ordering in pure $BaTiO_3$) matches the transformation from tetragonal to pseudocubic as indicated by the decrease in the *c/a* ratio and from permittivity data. However, the core regions of undoped BT are not detected by Raman spectroscopy because Raman is a *local* probe method, and the relative amounts of these regions of tetragonal BT is small compared to the surrounding pseudocubic phase.

V-Conclusions

A study of the $(1-x)$BaTiO$_3$-xBiGdO$_3$ system has been conducted for the first time. Gd can be incorporated into the BaTiO$_3$ matrix up to $x = 0.10$, as demonstrated by the trend in the lattice parameters and EDS results. However, as suggested by Rietveld refinements, BSE images and EDS analysis, samples often contain inhomogeneities. Bi and Gd form a stable secondary phase that fills the space between grains; diffusion of Bi into the BaTiO$_3$ matrix can be slower than the other two processes and incomplete. This inhomogeneity is reflected in the dielectric response, with two maxima suggesting the presence of a residual core/shell structure where dopants are confined to the outer grain regions, as observed directly in TEM. T$_C$ decreases with composition, until a ferroelectric-to-relaxor crossover occurs at $x = 0.08$, consistent with XRD patterns and Raman spectra. Co-doping with Bi and Gd thus first disrupts the long range ordering of ferroelectric BaTiO$_3$ and finally leads to typical relaxor behaviour, with a high relative permittivity maximum slightly below room temperature.

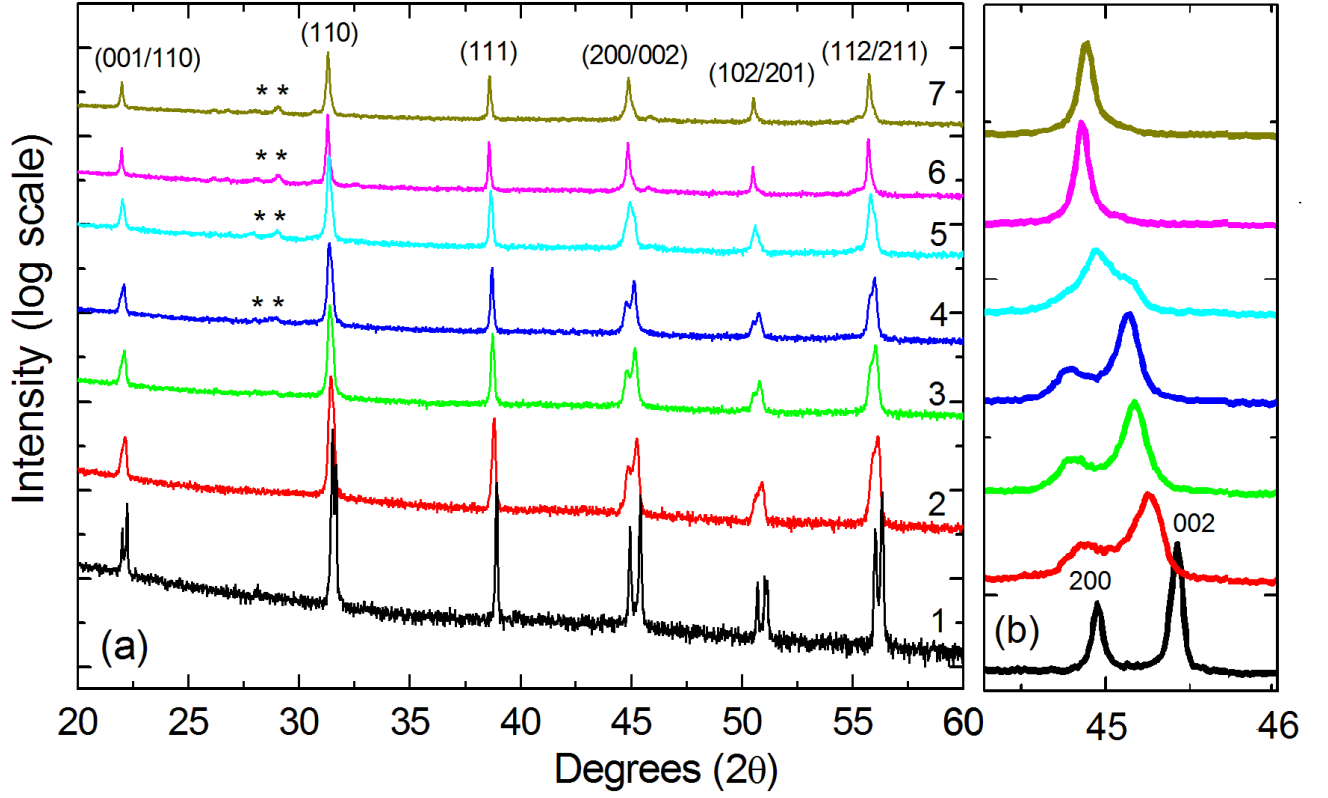**Fig. 1(a).** Room temperature XRD patterns for $(1-x)$BaTiO$_3$-xBiGdO$_3$ solid solutions (logarithmic scale): (1) $x = 0.00$, (2) $x = 0.02$, (3) $x = 0.04$, (4) $x = 0.06$, (5) $x = 0.08$, (6) $x = 0.10$, (7) $x = 0.15$ (* = Bi$_{1.55}$Gd$_{0.45}$O$_3$ - PDF no. 00-048-0351). **Fig. 1(b):** evolution of (200)/(002) peak splitting with composition.
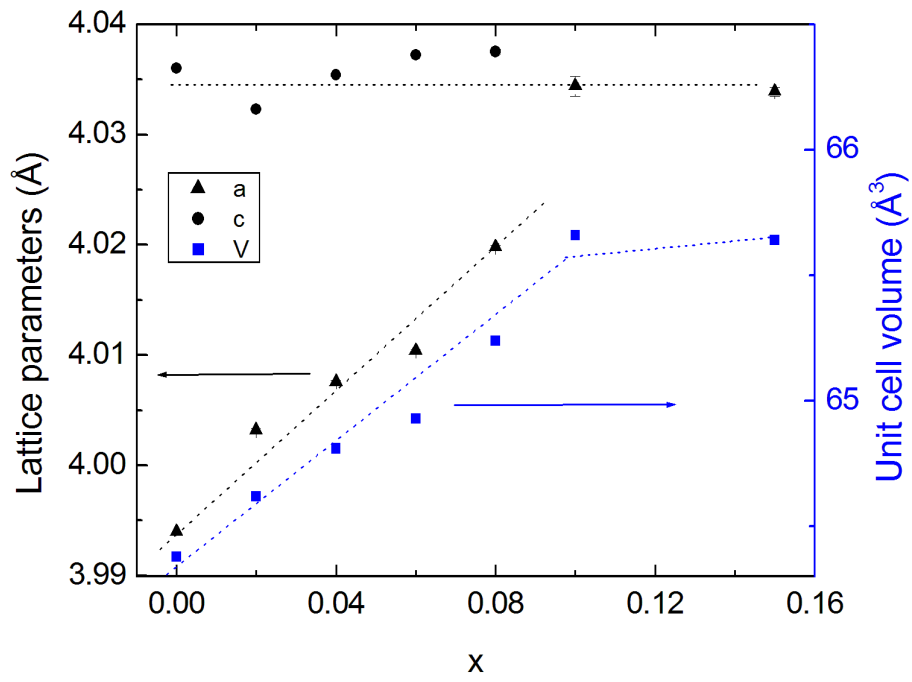
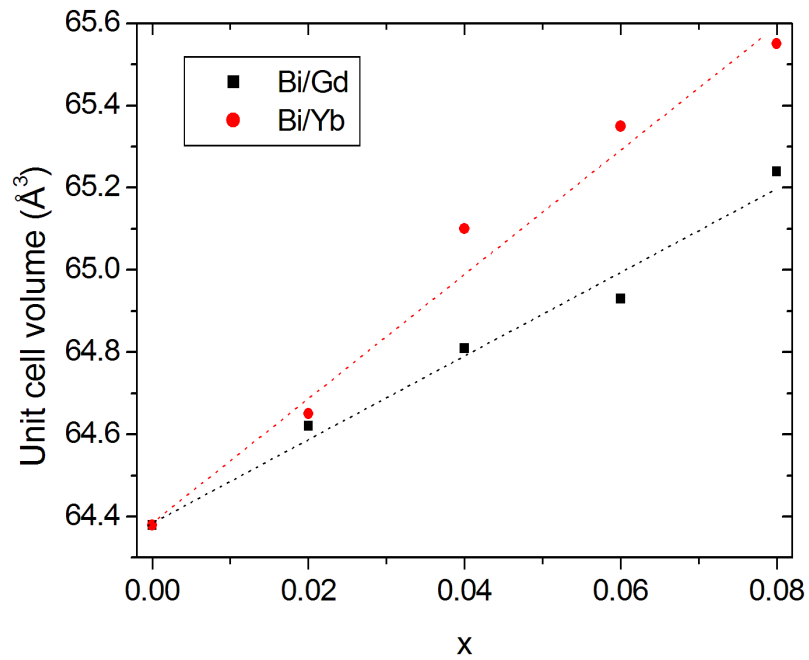**Fig. 2. Compositional dependence of lattice parameters and unit cell volume.**

Fig. 3. Comparison of unit cell volume between (1-x)BaTiO$_3$-xBiYbO$_3$ [11] and (1-x)BaTiO$_3$-xBiGdO$_3$ for $0 \leq x \leq 0.08$.
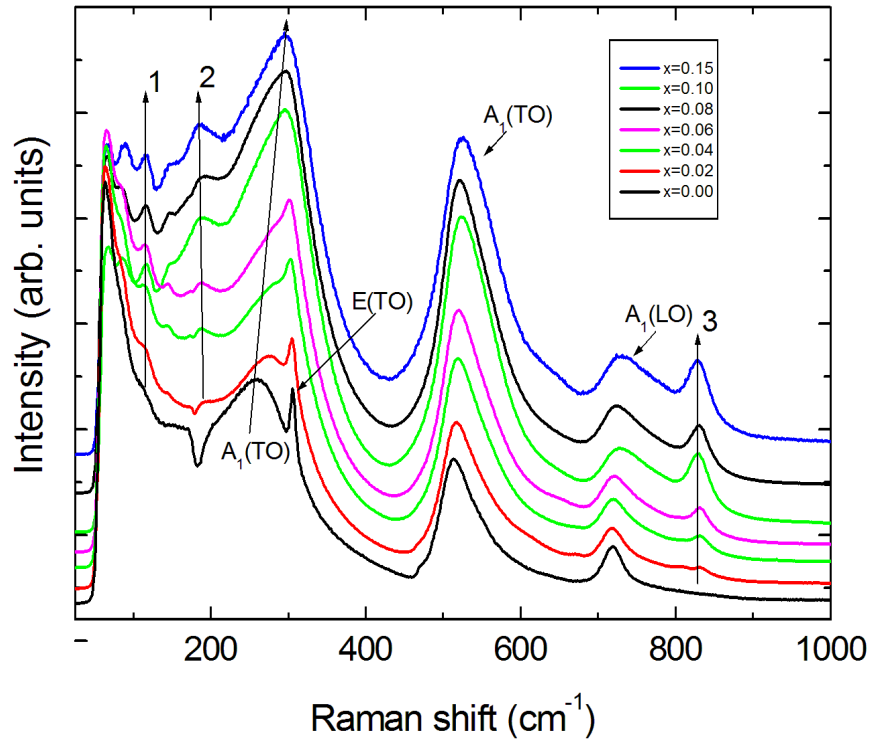
Fig. 4. Room temperature Raman spectra for (1-x)BaTiO₃-xBiGdO₃, *x* = 0.00 to 0.15 (from top to bottom).
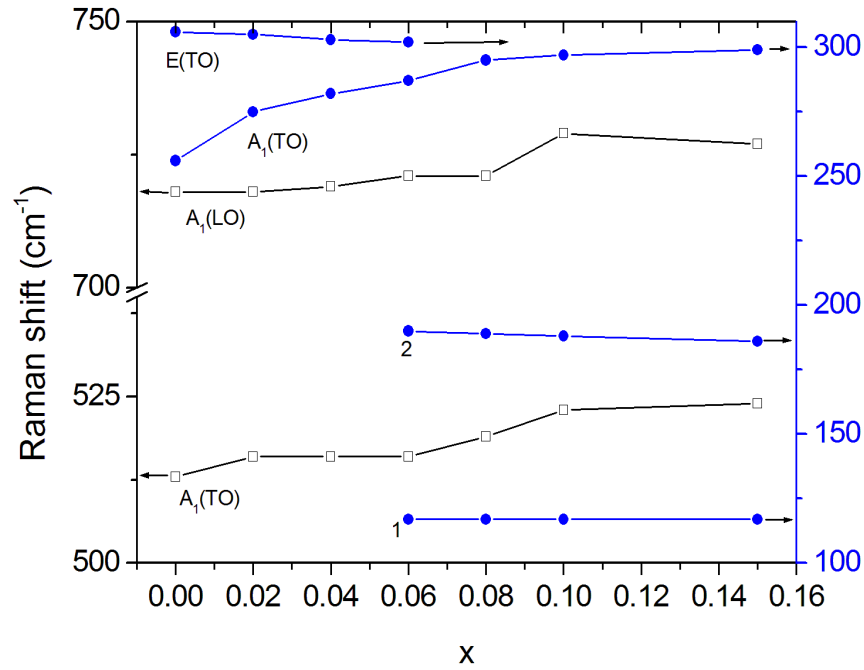

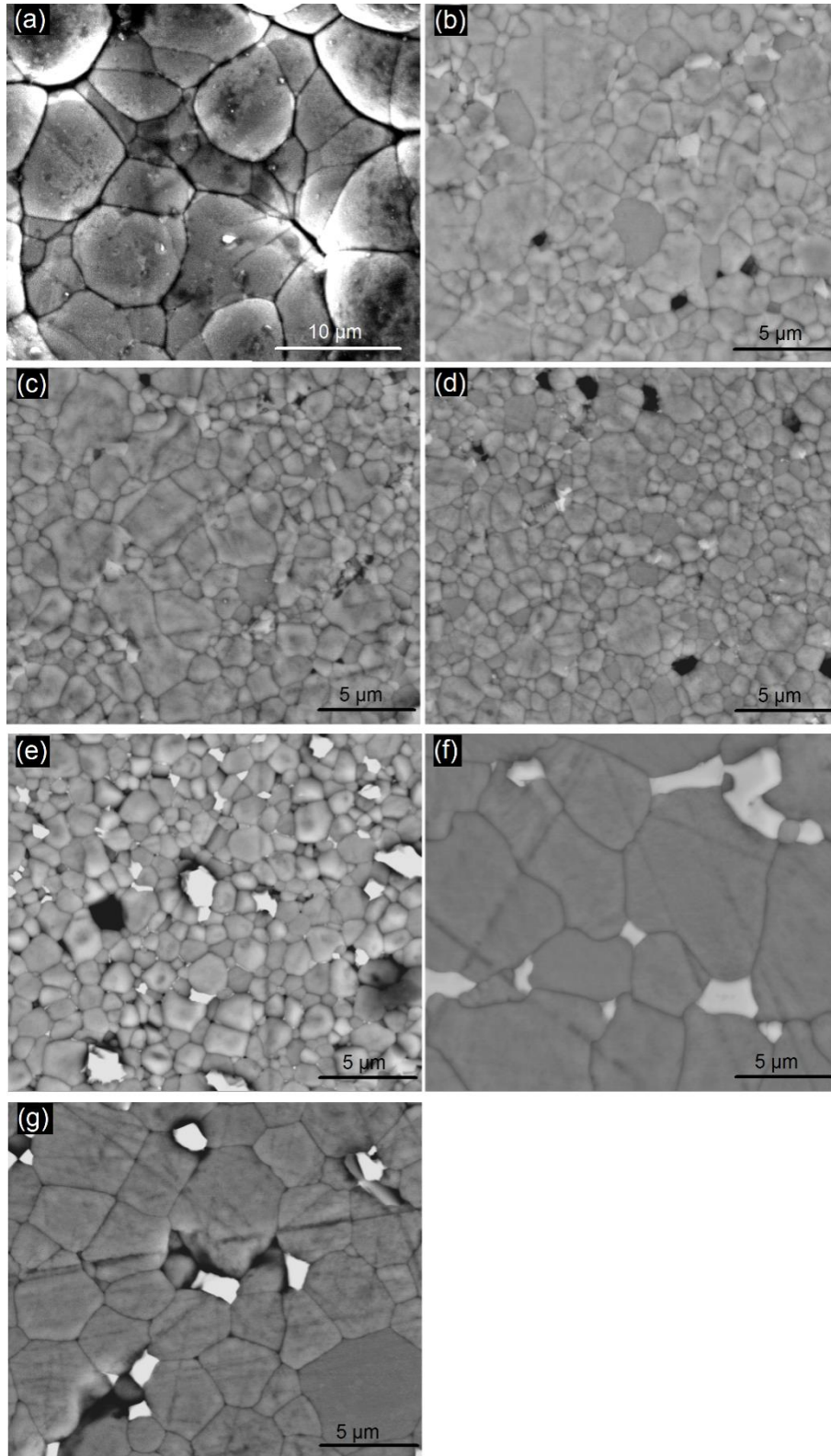**Fig. 5. Compositional dependence (*x*) of selected Raman modes.**

Fig. 6. SEM micrographs of ceramics sintered at (a-d) 1350 °C and (e-f) 1400 °C for 2 h, polished and thermally etched at 1200 °C for 30 minutes: (a) *x* = 0.00, (b) *x* = 0.02, (c) *x* = 0.04, (d) *x* = 0.06, (e) *x* = 0.08, (f) *x* = 0.10 and (g) *x* = 0.15.
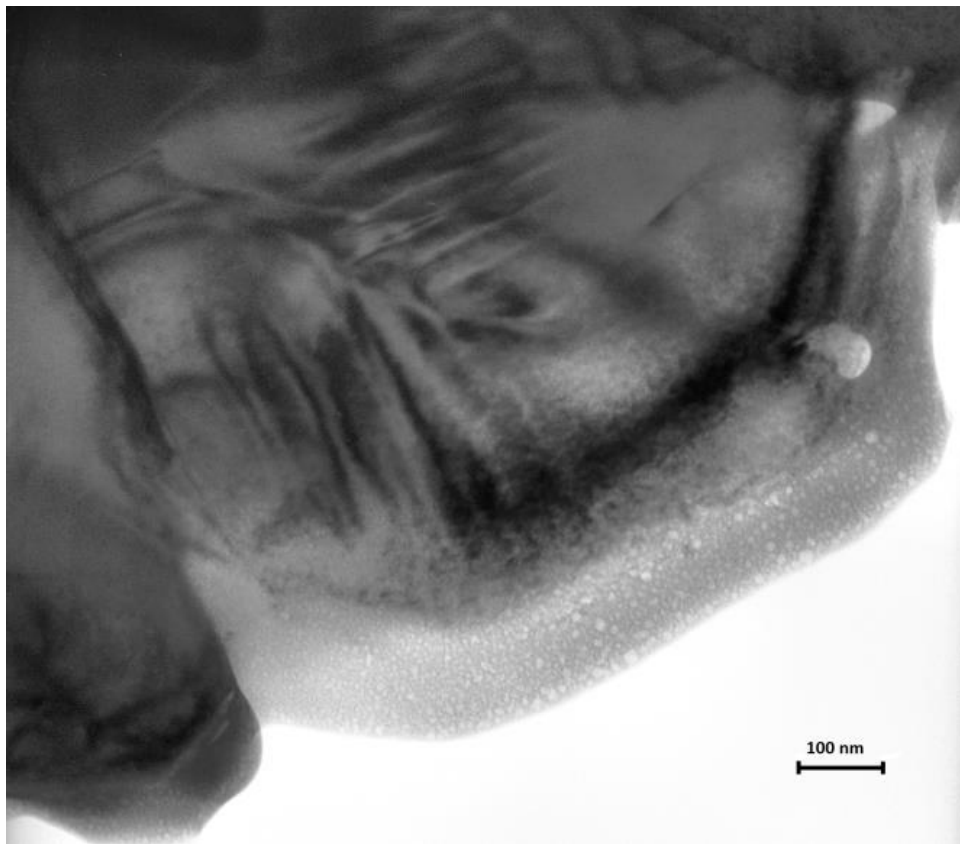
Fig. 7. TEM micrograph of composition $x = 0.10$ sintered at 1400 °C for 2 h, showing a core/shell structure.
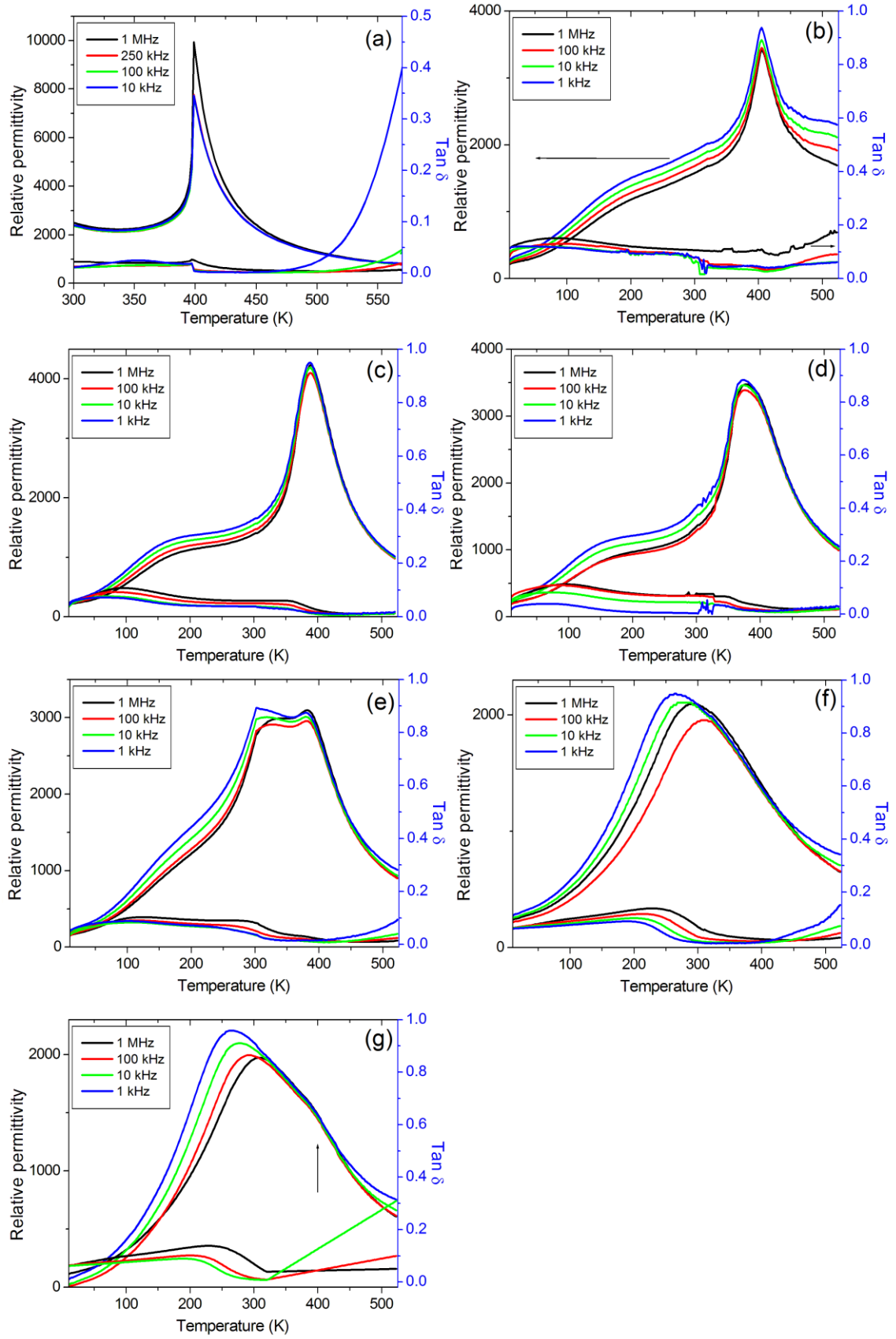
Fig. 8. Temperature dependence of the relative permittivity in the range 10-523 K for ceramics: (a) *x* **= 0.00, (b)** *x* **= 0.02, (c)** *x* **= 0.04, (d)** *x* **= 0.06, (e)** *x* **= 0.08, (f)** *x* **= 0.10 and (g)** *x* **= 0.15.**

Table 1. Lattice parameters, unit cell volume and *c/a* ratio for (1-x)BaTiO₃-xBiGdO₃, obtained from Rietveld refinements of room temperature XRD patterns (sintered pellets).

x	a (Å)		c (Å)	V (Å³)		*c/a* ratio
0.00	3.9910(2)		4.0319(2)	64.22(1)		1.01025
0.02	4.0032(1)		4.0323(2)	64.62(1)		1.00727
0.04	4.0076(1)		4.0354(1)	64.81(1)		1.00694
0.06	4.0104(1)		4.0372(2)	64.93(1)		1.00668
0.08	4.0198(2) Tetragonal	4.0291(1) Pseudocubic	4.0375(2)	65.24(1) Tetragonal	65.41(1) Pseudocubic	1.00440
0.10	4.0344(9)			65.66(4)		1
0.15	4.0339(4)			65.64(2)		1

Table 2. EDS analysis on (a) matrix grains and (b) on the secondary phase (white areas in BSE images); composition is given in at. % excluding oxygen.

Bulk (a)	0.02	0.04	0.06	0.08	0.10 Sint. t = 2h	0.10 Sint. t = 10h	0.15
Ti	47.9±0.5	48.6±1.1	46.2±0.9	45±0.3	44.0±0.8	45.4±0.3	43.9±0.7
Ba	49.8±0.5	47.9±0.5	48.2±0.6	49±0.6	48.8±0.5	47.7±0.5	49.3±0.5
Gd	1.43±0.21	2.1±0.2	3.6±0.6	4.3±0.7	5.3±0.7	5.3±0.3	5.2±0.4
Bi	0.85±0.12	1.4±0.2	2.1±0.9	1.3±0.4	1.8±1.0	1.7±0.3	1.6±0.2

Secondary phase (b)	0.08	0.10 Sint. t = 10h	0.15
Ti	23.8±1.6	4.7±1.8	3.2±0.1
Ba	24.9±2.0	4.5±2.2	2.5±0.2
Gd	16.2±1.1	33.7±1.4	23.9±0.1
Bi	35.1±2.5	57.1±2.7	70.5±0.1

Table 3. Comparison of ionic radii and solid solution limits for (*1-x*)BaTiO₃-*x*Bi[Me^III]O₃.

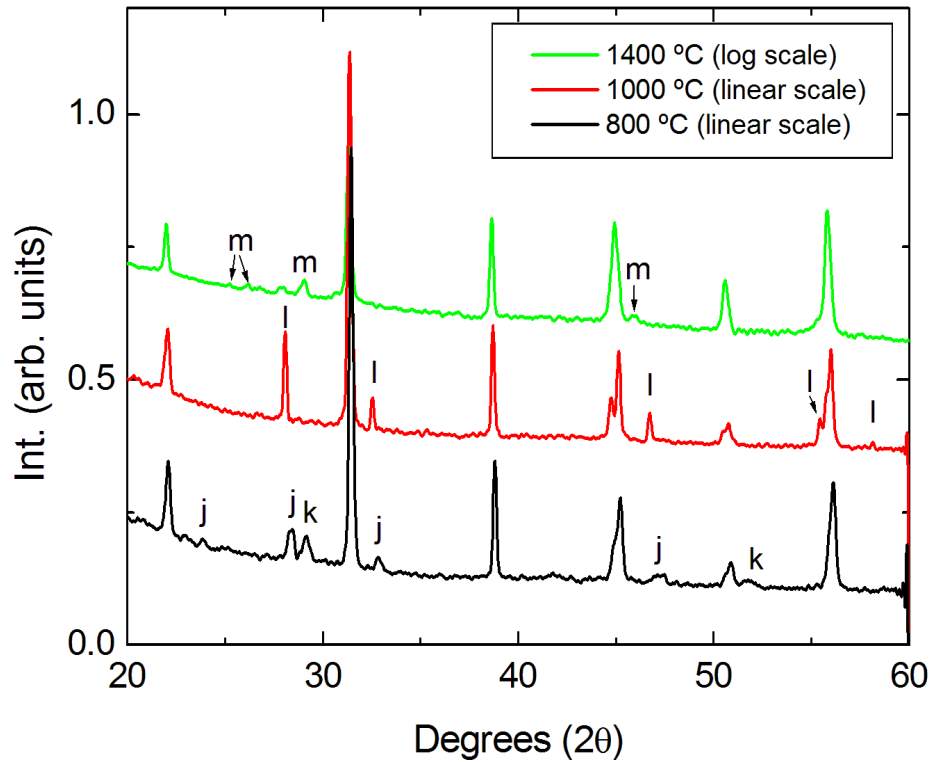|	radius (nm)	solid solution limit	Ref.
Al	0.535	12%	[8]
In	0.68	25%	[10]
Sc	0.745	40%	[9]
Yb	0.868	30%	[11]
Gd	0.938	10%	[This study]

Fig. 9. Evolution of parasitic phases with sintering temperature (x = 0.10); j = Bi_2O_3 (PDF no. 01-076-2478), k = Gd_2TiO_5 (PDF no. 00-034-1307), l = $Bi_{1.208}Gd_{0.792}O_3$ (PDF no. 00-040-0318), m = $Bi_{1.55}Gd_{0.45}O_3$ (PDF no. 00-048-0351).

References

1. A. von Hippel, R. G. Breckenridge, F. G. Chesley and L. Tisza, 'High dielectric constant ceramics,' Industrial & Engineering Chemistry, 38 [11] 1097-1109 (1946).

2. J. G. Powles and W. Jackson, 'The measurement of the dielectric properties of high-permittivity materials at centimetre wavelengths,' Proceedings of the IEE - Part III: Radio and Communication Engineering, 96 [43] 383-389 (1949).

3. A. Von Hippel, 'Dielectric Materials and Applications'.Technology Press of MIT, Cambridge, US, 1954.

4. R. Cohen, 'Origin of ferroelectricity in perovskite oxides
,' Nature, 358 [6382] 136-138 (1992).

5. A. Feteira and D. C. Sinclair, 'The influence of nanometric phase separation on the dielectric and magnetic properties of (1-x)BaTiO_3-xLaYbO_3 (0 $\leq$ x $\leq$ 0.60) ceramics,' J. Mater. Chem., 19 [3] 356-359 (2009).

6. M. C. Ferrarelli, C. C. Tan and D. C. Sinclair, 'Ferroelectric, electrical, and structural properties of Dy and Sc co-doped $BaTiO_3$,' J. Mater.Chem., 21 [17] 6292-6299 (2011).

7. G. Shirane and K. Suzuki, 'On the Phase Transition in Barium-Lead Titanate (1),' J. Phys. Soc. Jpn., 6 [4] 274-278 (1951).

8. Huichun Yu and Zuo-Guang Ye, 'A new relaxor ferroelectric system of $(1-x)BaTiO_3-xBiAlO_3$ solid solution,' Applications of Ferroelectrics, 2008. ISAF 2008.17th IEEE International Symposium on the, 1 1-2 (2008).

9. H. Ogihara, C. A. Randall and S. Trolier-McKinstry, 'Weakly Coupled Relaxor Behavior of $BaTiO_3-BiScO_3$ Ceramics,' J. Am. Ceram.Soc., 92 [1] 110-118 (2009).

10. K. Datta, E. Suard and P. A. Thomas, 'Compositionally driven ferroelectric phase transition in $xBiInO_3$ - $(1-x)BaTiO_3$: A lead-free perovskite-based piezoelectric material,' Appl. Phys. Lett., 96 [22] 221902 (2010).

11. T. Strathdee, L. Luisman, A. Feteira and K. Reichmann, 'Ferroelectric-to-relaxor crossover in $(1-x)BaTiO_3-xBiYbO_3$ $(0 \leq x \leq 0.08)$ ceramics,' J. Am. Ceram. Soc., 94 [8] 2292-2295 (2011).

12. R. D. Shannon, 'Revised Effective Ionic Radii and Systematic Studies of Interatomic Distances in Halides and Chalcogenides,' ActaCryst., A32 751 (1976).

13. V. Goldschmidt, 'Shrifter Norske Videnskop-Akad.' (Nov 1926).

14. A. C. Larson and R. B. Von Dreele, 'General Structure Analysis System (GSAS),' Los Alamos National Laboratory Report LAUR, 86 748 (1994).

15. L. B. McCusker, R. B. Von Dreele, D. E. Cox, D. Louër and P. Scardi, 'Rietveld refinement guidelines,' J. Appl. Crystall., 32 [1] 36-50 (1999).

16. G. Schileo, L. Luisman, A. Feteira, M. Deluca and K. Reichmann, 'Structure–property relationships in $BaTiO_3$–$BiFeO_3$–$BiYbO_3$ ceramics,' J. Eur. Ceram.Soc., 33 [8] 1457-1468 (2013).

17. Y. Shiratori, C. Pithan, J. Dornseiffer and R. Waser, 'Raman scattering studies on nanocrystalline $BaTiO_3$ Part II—consolidated polycrystalline ceramics,' J. Raman Spectrosc., 38 [10] 1300-1306 (2007).

18. M. Frey, Z. Xu, P. Han and D. Payne, 'The role of interfaces on an apparent grain size effect on the dielectric properties for ferroelectric barium titanate ceramics,' Ferroelectrics, 206 [1-4] 337-353 (1998).

19. J. Pokorny, U. Pasha, L. Ben, O. Thakur, D. C. Sinclair and I. M. Reaney, 'Use of Raman spectroscopy to determine the site occupancy of dopants in BaTiO3,' J. Appl. Phys., 109 [11] 114110 (2011).

20. P. Su and A. V. Virkar, 'Subsolidus Phase Diagram of the Bi_2O_3-Gd_2O_3 System and the Morphology of Phase Separation,' J Am Ceram Soc, 82 [8] 2225-2232 (1999).